

SWEEP ANGLE STUDY OF A STRUT-BRACED-WING REGIONAL JET WITH NATURAL LAMINAR FLOW

Nathalie Sa'adeh[1] & David W. Zingg[1]

[1]Institute for Aerospace Studies, University of Toronto, Toronto, Ontario, M3H 5T6, Canada

Abstract

The strut-braced-wing configuration with natural laminar flow has the potential to achieve significant fuel-burn reduction relative to conventional aircraft. While a few studies have investigated the extent of this potential at modest cruise speeds, further work is required to explore this concept at conventional transonic cruise speeds, necessitating substantial sweep angles that typically destabilize crossflow instabilities. In this paper, a sweep angle study of a strut-braced-wing regional jet operating at Mach 0.78 is performed using aerodynamic shape optimization based on the Reynolds-averaged Navier-Stokes equations, coupled with the SA-sLM2015cc transport-equation-based transition model. Single-point optimizations are performed for sweep angles of 28°, 26°, 24°, and 22°, to determine the effects of sweep angle on the extent of laminar flow and overall drag. The optimizations account for transition due to both Tollmien-Schlichting and crossflow instabilities. Results show that reducing the sweep angle leads to slightly higher optimal cruise altitudes, while the total cruise drag remains nearly constant. The largest difference comes from the drag breakdown, where reducing the sweep angle decreases friction drag due to increased regions of laminar flow and lower dynamic pressures, while wave drag increases.

Keywords: Strut-braced wing, natural laminar flow, aerodynamic shape optimization

1. Introduction

As air traffic demands continue to increase, there is a growing necessity to limit aviation's impact on climate change and achieve net-zero carbon emissions from aircraft operations by 2050. Advancing designs of fuel-efficient next-generation aircraft is at the forefront of such efforts, including the exploration of unconventional aircraft configurations. One configuration receiving much attention is the strut-braced-wing (SBW) concept, which features a large wingspan supported by struts that alleviate root bending moments caused by aerodynamic loading [1]. This high-aspect-ratio configuration yields lower induced drag, with thinner wing cross sections that reduce its susceptibility to wave drag. For a given wing area, the structural efficiency of the struts also allows for shorter chord lengths [2]. On its own, the SBW concept provides aerodynamic advantages over conventional tube-and-wing designs [3]; however, it has the potential to further reduce drag by maintaining a large extent of laminar flow over the wings and strut, which can be passively achieved through natural laminar flow (NLF). This design approach uses shape design to delay boundary-layer transition by obtaining pressure distributions capable of suppressing the growth of instabilities. For swept-wing aircraft, the two dominant instabilities are Tollmien-Schlichting (TS) and crossflow modes, which require opposing pressure distributions for suppression. Moreover, the high sweep angles necessary to minimize wave drag at transonic speeds destabilize crossflow instabilities, thereby presenting further design challenges [4]. Despite these challenges, the SBW configuration lends itself as a promising baseline for the application of NLF, as its inherent wing structure allows it to operate at lower chord Reynolds numbers relative to conventional aircraft, and its thinner wing sections provide the potential to reduce its sweep angle [2].

https://doi.org/10.71945/icas2026_0066

Boeing and NASA investigated a transonic truss-braced-wing (TTBW) single-aisle aircraft, which is a variation of an SBW aircraft that includes one or more jury struts to provide further structural efficiency in exchange for lower aerodynamic efficiency [5]. As part of the second phase of the Subsonic Ultra-Green Aircraft Research (SUGAR) program, they analyzed the application of NLF to their TTBW for a cruise altitude of 45,000 ft, corresponding to a lift coefficient of 0.70, and a cruise speed of Mach 0.70. Their framework incorporates the aerodynamic effects of NLF with prescribed transition locations. When applying NLF on both the upper and lower wing surfaces of their TTBW, their optimum configuration yields a lift-to-drag (L/D) ratio of approximately 31 [5]. Sa'adeh and Zingg [6] investigated the design of a transonic SBW regional jet with NLF (SBW100-NLF) for a cruise speed of Mach 0.78, cruise altitudes of 44,670 ft and 37,000 ft, and wing sweep angles ranging from 30° to 26°. Through lift-constrained drag minimization, they showed that the SBW100-NLF with 28° sweep operating at a cruise speed typical of current regional and single-aisle class aircraft can achieve similar aerodynamic performance to Boeing and NASA's TTBW design, with an L/D of 29, excluding drag from the vertical tail, nacelles, and pylons. They noted that while operation at the higher cruise altitude results in better aerodynamic performance for the SBW100-NLF aircraft, operation at the lower cruise altitude maintains more laminar flow.

The objective of this paper is to investigate sweep angle effects on the extent of laminar flow and overall cruise drag of a transonic strut-braced-wing regional jet with natural laminar flow operating at a cruise speed of Mach 0.78. High-fidelity aerodynamic shape optimization with integrated transition prediction is used to identify the optimal altitude and corresponding geometry that minimizes cruise drag for specified sweep angles of a strut-braced-wing regional jet, extending the previous investigations of Sa'adeh and Zingg [6].

2. Methodology

High-fidelity aerodynamic shape optimization of the SBW100-NLF aircraft with sweep angles of 28°, 26°, 24°, and 22° is performed using Jetstream, a framework developed at the University of Toronto. The optimization framework consists of an integrated geometry parameterization and mesh deformation scheme [7], geometry control through free-form and axial curve deformation [8], a Newton-Krylov-Schur flow solver for the Reynolds-averaged Navier–Stokes (RANS) equations [9] with a local correlation-based transition prediction model, the SA-sLM2015cc model [10], coupled to the Spalart-Allmaras (SA) turbulence model [11], and a gradient-based optimization algorithm, SNOPT [12], with gradients computed via the discrete-adjoint method. A brief description of each component is provided.

2.1 Geometry Parameterization and Mesh Deformation

Following geometric deformation during optimization, the computational mesh must be updated. Jetstream uses an integrated approach to accomplish this task, with B-spline patches and volumes used to analytically represent the geometry and parameterize each block of the surrounding multiblock structured mesh [7]. Each block of the initial mesh is approximated using cubic B-spline volumes defined by their control points. The resulting B-spline control grid, representing a coarser computational mesh, is then used by the mesh-deformation algorithm during optimization [7, 13]. Through linear elasticity equations, deformations applied to surface control points are propagated across the control volume of each corresponding block, thus deforming the computational grid [7, 13].

2.2 Geometry Control

Free-form deformation (FFD) volumes and axial curves are used to control the shape of aerodynamic surfaces during optimization. FFD volumes are B-spline volumes that embed the parameterized aerodynamic surfaces; therefore, perturbations applied to their control points deform the embedded geometry [8]. In wing optimization, these control points are used to control twist, taper, and section shape. The geometry control system of the SBW100-NLF aircraft is shown in Figure 1, where the wing, strut, and tail are each embedded within their respective FFD volumes. The control points of each FFD are arranged in cross-sections, consisting of 11 control-point pairs. An axial curve,

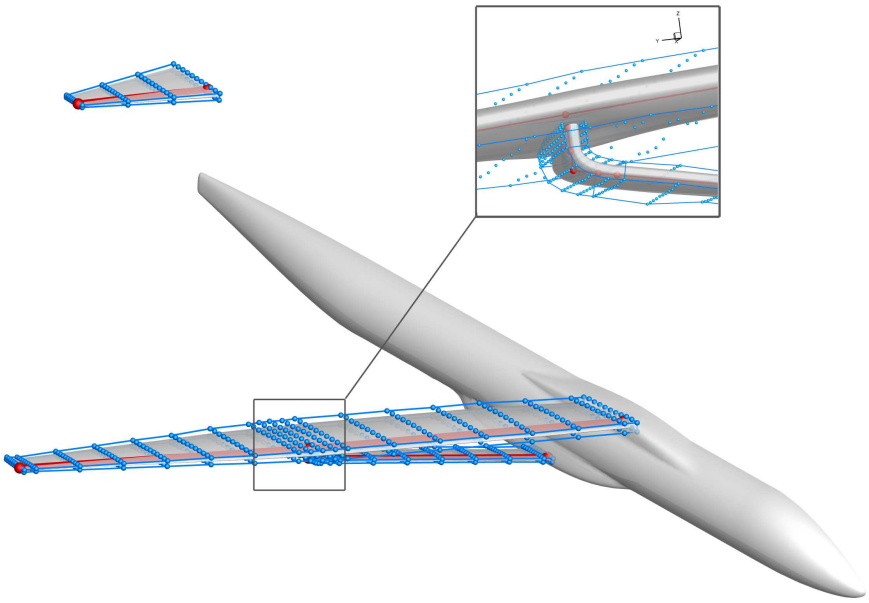


Figure 1 – Geometry control system of the SBW100-NLF aircraft, with FFD volumes shown in blue and axial curves in red.

defined at the quarter-chord of each FFD volume and represented as a B-spline curve, enables global changes such as sweep, span, and dihedral [8].

2.3 RANS Flow Solver

Jetstream's flow solver, which is applicable to multiblock structured meshes, is based on an implicit Newton-Krylov algorithm with a Schur complement method for parallel preconditioning [9, 14]. Spatial discretization is implemented using second-order centered-difference summation-by-parts operators, with simultaneous approximation terms used to enforce boundary conditions and couple block interfaces [9].

2.4 Transition Prediction Model

The transition prediction model integrated into Jetstream, termed SA-sLM2015cc model, was developed by Piotrowski and Zingg [15]. Their model is based on the Langtry–Menter γ–$\tilde{Re}_{\theta t}$ transition model [16], modified to enable coupling with the one-equation SA turbulence model. It relies on empirical correlations for TS instabilities developed by Langtry and Menter [17], as well as local helicity-based crossflow correlations from Langtry et al. [16]. These correlations are incorporated into two transport equations: the first governs the intermittency, γ, which triggers transition by controlling the turbulence level within the boundary layer. The second governs the transition momentum-thickness Reynolds number, $\tilde{Re}_{\theta t}$, which diffuses from the freestream into the boundary layer and determines the onset of transition [17]. In addition to introducing smooth approximations to non-differentiable functions within the two transport equations [10], which is critical for both solver and optimization convergence, Piotrowski and Zingg [15] extended their transition model to transonic flow by developing and implementing compressibility corrections for TS and crossflow instabilities. This allows their model to account for the stabilizing effects of higher Mach numbers on each mechanism independently [15]. The SA-sLM2015cc model was used for previous SBW100-NLF optimizations, as found in [6], and is also used in the current work.

2.5 Gradient-Based Optimization

The well-established Sparse Nonlinear OPTimizer (SNOPT) package [12] is integrated into Jetstream to perform aerodynamic shape optimization. SNOPT is a gradient-based optimizer that uses a sequential quadratic programming algorithm with a quasi-Newton BFGS approximation to the Hessian

Table 1 – Lift-to-drag maximization results of the SBW100-NLF aircraft with 28° sweep.

	D^1 [lb]	D_p [lb]	D_f [lb]	C_L	L [lb]	Altitude (ft)	L/D^1	AOA	Λ
SBW100 fully turbulent optimum	3,975	2,118	1,857	0.68	97,000	44,670	24.4	2.96°	30°
SBW100-NLF L/D maximization	3,348	1,787	1,560	0.67	96,820	44,350	28.9	2.86°	28°
SBW100-NLF / SBW100	-15.8%	-15.6%	-16.0%	-	-180	-320	+18.5%	-	-

[1] Excrescence drag markup and drag contributions from the vertical tail, nacelles, and pylons are not included.

of the Lagrangian, enabling efficient exploration of the design space until convergence to a locally optimal solution [18]. The discrete-adjoint method provides SNOPT with the gradients of the objective function and flow-dependent nonlinear constraints [19].

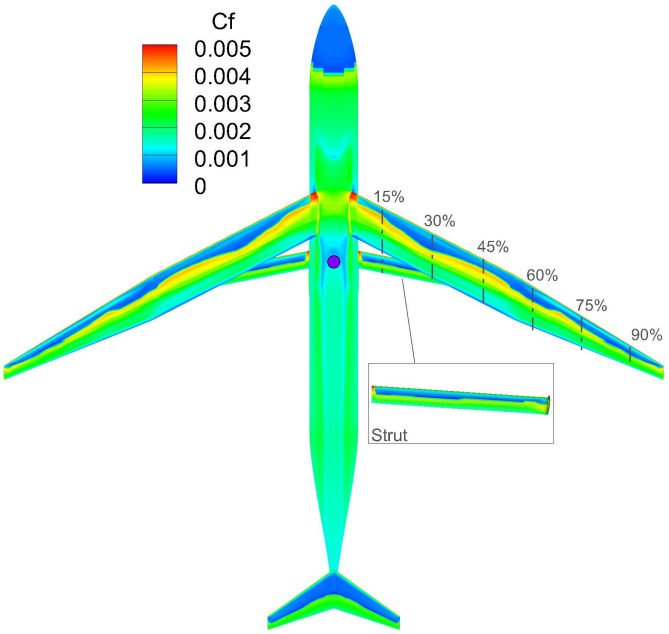
3. Single-Point Optimization Results

Four L/D maximizations of the SBW100-NLF are performed, with each case representing a wing sweep angle ranging from 22° to 28°, at a cruise speed of Mach 0.78 and a Reynolds number of 9.92×10^6. The mission capabilities of this aircraft are based on those of the Embraer E190-E2 regional jet [20], including a payload of 104 PAX over a nominal range of 500 nmi. The computational grid used for the optimizations has 26.51 million nodes, consistent with that used by Chau and Zingg [3], as well as Sa'adeh and Zingg [6]. The design variables for all cases include the angle of attack, geometric design variables to control the section shape and twist for the wing and strut, as well as the tail incidence angle. While the sweep angle changes between each case, it is left fixed during each optimization, as the geometry parameterization and mesh deformation at the wing-strut junction pose difficulties if it were free to vary. The span and dihedral are also frozen during the optimizations to preserve aircraft characteristics that affect the structural performance of the wing. A trim constraint is included to ensure zero pitching moment, while thickness constraints are used to satisfy the structural requirements previously imposed by Chau and Zingg [3] during the development of the fully turbulent optimized SBW100. In addition, a minimum volume constraint is implemented to ensure sufficient fuel-tank capacity, as fuel is assumed to be stored in the wing and strut.

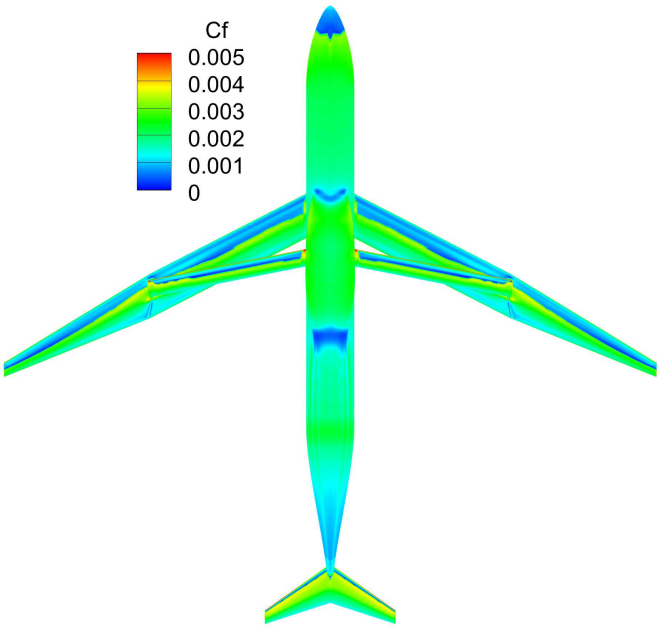
3.1 28° Sweep Angle

A single-point optimization of the SBW100-NLF aircraft with 28° sweep is performed with the objective of maximizing L/D. The results of this optimization are shown in Table 1, which includes the total cruise drag, along with the pressure and skin-friction breakdown. These drag values take into account the change in aircraft weight when reducing the sweep angle, where the change in wing weight was computed using Raymer's empirical equation [21]. The results are compared to those obtained from lift-constrained drag minimization of the fully turbulent SBW100 aircraft performed by Chau and Zingg [3], for which they specified a cruise altitude of 44,670 ft, corresponding to a lift coefficient of 0.68. An L/D maximization of this baseline configuration was not performed, as this cruise altitude was determined to be optimal for the fully turbulent SBW100 during the conceptual design phase.

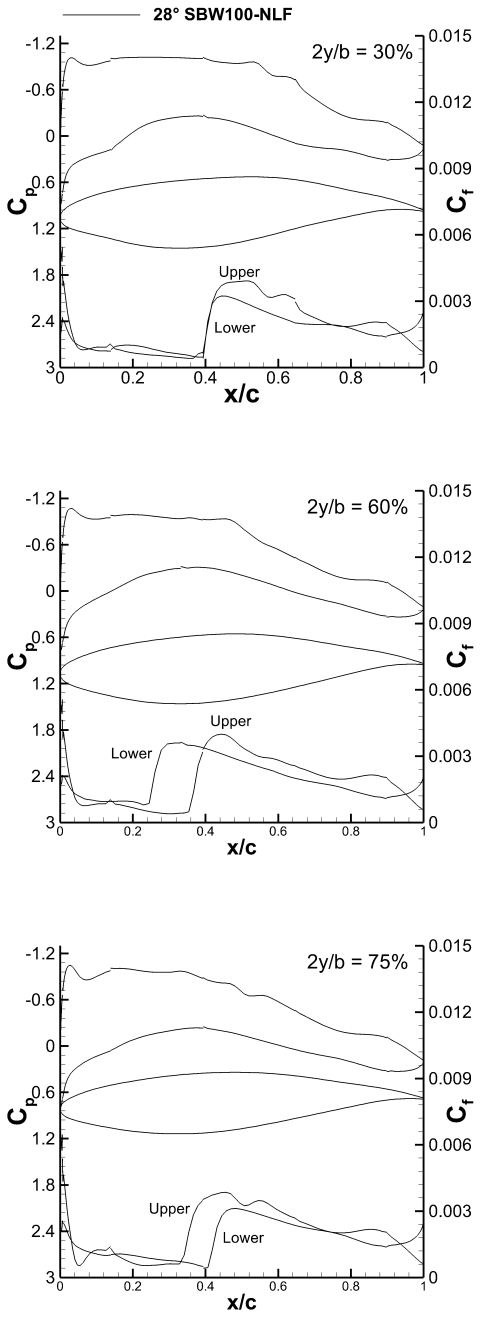
When the optimizer is not constrained to meet a target lift coefficient, it converges to an optimal lift coefficient value of 0.67, corresponding to an optimal altitude of 44,350 ft for the SBW100-NLF with 28° sweep. This results in a 15.8% reduction in the total cruise drag relative to the fully turbulent SBW100, with an approximately equal reduction in both pressure and skin-friction drag components. The skin-friction contours of the upper and lower surfaces for the 28° sweep L/D optimum are shown in Figures 2a and 2b, respectively, where dark blue denotes laminar flow. The pressure and skin-friction distributions, C_P and C_f, for the 30%, 60%, and 75% spanwise stations along the wing are shown in Figure 2c, where a sharp increase in the C_f plot corresponds to transition. As seen from the upper-surface skin-friction contour and distributions, laminar flow is sustained up to approximately 35–40% chord at all three spanwise stations. The lower surface also maintains laminar flow up to 40% chord, with the exception of the 60% spanwise station, which is located near the wing-strut junction at 55% span. The laminar flow sustained along the lifting surfaces of the aircraft reduces viscous drag through reductions in both skin-friction and form drag. In addition, part of the reduction



(a) Upper surface and CG shown as purple circle



(b) Lower surface



(c) Pressure and skin friction profiles

Figure 2 – Lift-to-drag maximization of the SBW100-NLF aircraft with 28° sweep.

in the pressure drag component is also attributed to a decrease in induced drag driven by higher dynamic pressure at lower altitude combined with a slight decrease in weight.

The location of the center of gravity (CG) is also shown in upper-surface skin-friction contour, represented by a purple circle. It should be noted that reducing the sweep angle shifts both the CG and neutral point forward, resulting in an overall reduction in static margin. This affects the trim drag contribution and longitudinal stability of the aircraft; however, this effect is ignored in the present study, and maintaining a fixed static margin while reducing the sweep angle is left for future work.

Table 2 – Lift-to-drag maximization results of the SBW100-NLF aircraft with 26° sweep.

	D^1 [lb]	D_p [lb]	D_f [lb]	C_L	L [lb]	Altitude (ft)	L/D^1	AOA	Λ
SBW100 fully turbulent optimum	3,975	2,118	1,857	0.68	97,000	44,670	24.4	2.96°	30°
SBW100-NLF 28° Sweep	3,348	1,787	1,560	0.67	96,820	44,350	28.9	2.86°	28°
SBW100-NLF L/D maximization	3,355	1,856	1,499	0.70	96,660	45,300	28.8	2.24°	26°
SBW100-NLF / SBW100 turbulent	-15.6%	-12.4%	-19.3%	-	-340	+630	+18.0%	-	-
SBW100-NLF / SBW100-NLF 28° Sweep	+0.2%	+3.8%	-3.9%	-	-160	+950	-0.35%	-	-

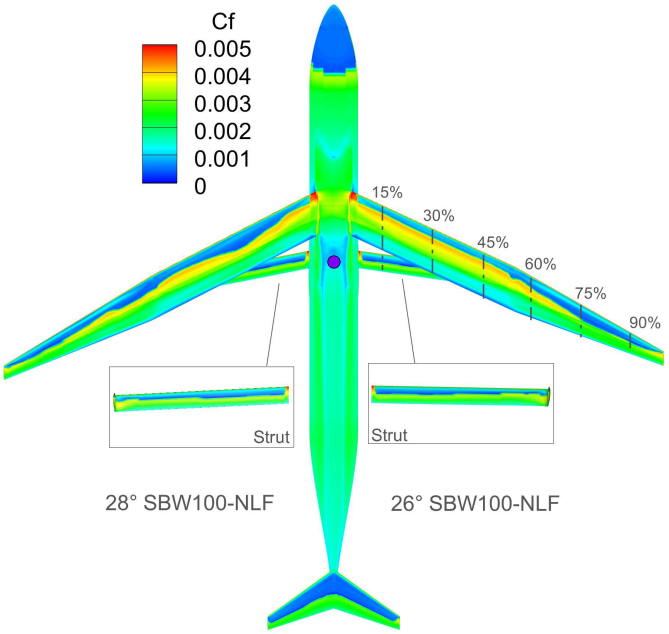
[1] Excrescence drag markup and drag contributions from the vertical tail, nacelles, and pylons are not included.

3.2 26°, 24°, and 22° Sweep Angles

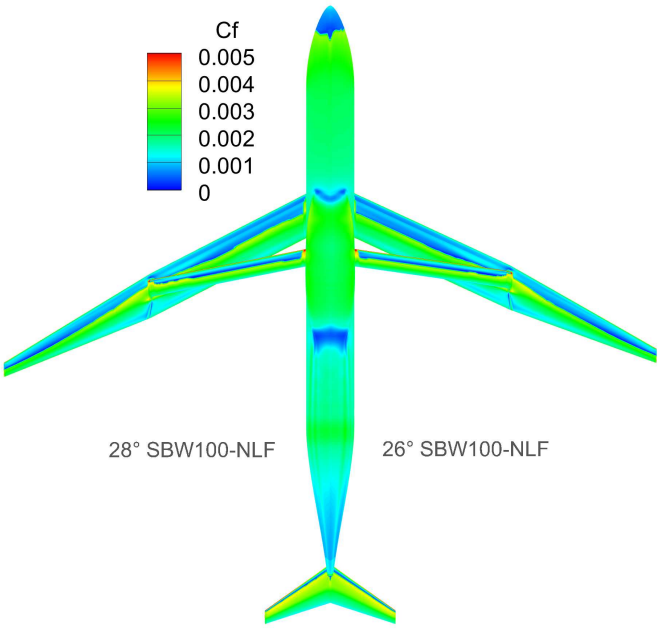
L/D maximizations for reduced sweep angles of 26°, 24°, and 22° for the SBW100-NLF are also performed. Table 2 provides comparisons of the results for the 26° sweep angle case with those of the fully turbulent SBW100 and the 28° sweep SBW100-NLF aircraft. Unlike the 28° sweep angle case, when reducing the sweep angle to 26°, the optimizer increases the lift coefficient from the baseline of 0.68 to 0.70, with a corresponding increase in the optimal cruise altitude. This configuration achieves a similar total cruise drag reduction to the 28° case, with 15.6% reduction relative to the fully turbulent SBW100. However, there are differences in the drag breakdown, as the 26° case achieves greater reductions in skin-friction drag and smaller reductions in pressure drag than the 28° case. The skin-friction contours for the 26° case are shown in Figures 3a and 3b, which are compared to those of the 28° case. It is evident that there is less laminar flow along the inboard and midspan regions of the upper wing surface for the 26° case relative to 28°. However, more laminar flow is observed over the outboard regions of the upper wing surface. These findings are corroborated by the skin-friction distributions in Figure 3c, where the upper surface transitions upstream at the 30% and 60% spanwise stations, and downstream at the 75% station. The pressure distribution at the outboard station for the 26° case features a near-zero pressure gradient along the chord that extends farther downstream than in the 28° case. While this promotes laminar flow over the outboard wing by stabilizing both TS and crossflow instabilities, it reduces the extent of the pressure recovery region, consequently leading to stronger shocks and increased wave drag penalties. In combination with an increase in induced drag from the lower dynamic pressure, this likely explains why the 26° case achieves less pressure-drag reduction than the 28° case relative to the baseline SBW100. Furthermore, there is little change in the extent of laminar flow along the lower wing surface and the strut; the reduction in skin-friction drag is attributed to the reduced air density at higher altitudes.

As the sweep angle is reduced to 24° and 22°, similar trends to those observed in the 26° case are apparent. The drag breakdowns of each case compared to the fully turbulent SBW100 and the 28° sweep SBW100-NLF are outlined in Tables 3 and 4, where the skin-friction drag continues to decrease, while the pressure drag increases relative to the 28° case. Similar to the 26° case, reductions in pressure drag are limited by wave drag penalties from strengthened shocks, as well as the increased induced drag contribution. The former are evident in the upper-surface pressure distributions across all spanwise stations for both 24° and 22° cases, shown in Figures 4c and 5c, respectively. The start of pressure recovery along the upper surface continues to shift downstream as the location of maximum thickness moves aft along the chord with decreasing sweep angle. This provides an advantage in extending laminar flow, but only in the outboard region. Along the inboard and midspan regions of the upper surface, the strong favourable pressure gradient following the leading edge likely triggers crossflow-induced transition, which is dominant in these regions. The lower surface favourable pressure gradient is strengthened as the sweep angle is further reduced, which helps to stabilize midchord TS instabilities and delay transition along the lower surface.

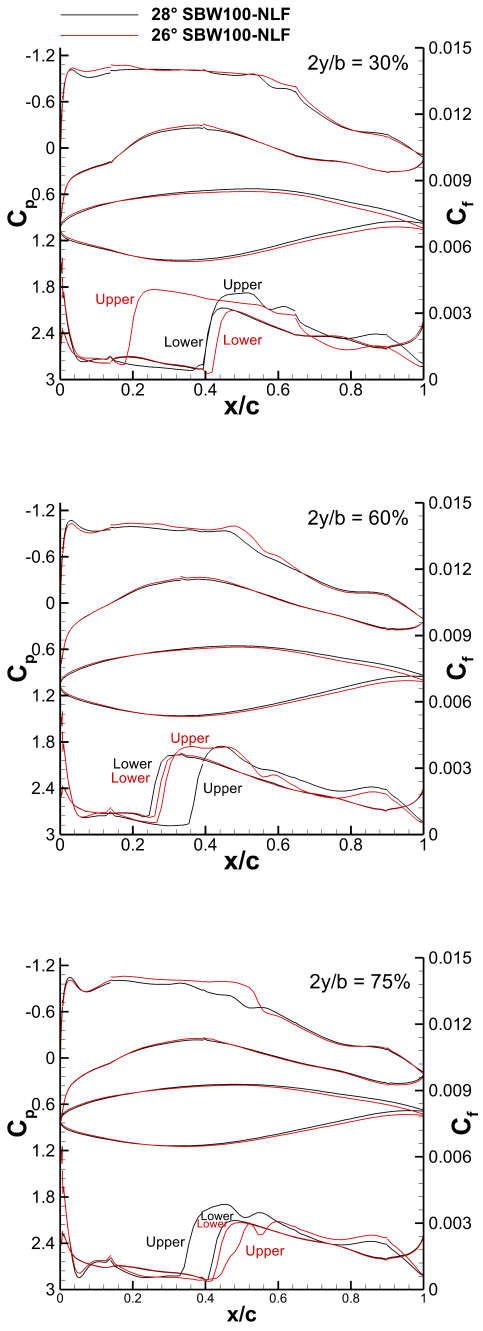
The trend of increasing optimal cruise altitude with decreasing sweep angle continues for the 24° case, but appears to plateau for the 22° case. On the other hand, the angle of attack decreases with decreasing sweep angle despite the increase in the cruise lift coefficient. This is accompanied by reduced leading-edge pressure peaks across all spanwise stations, which is most prominent in the 22° case. The changes in the cross-sectional shapes and angle of attack as the sweep angle is reduced leads to variations in the spanwise lift distribution, which is plotted for the 28° and 22°



(a) Upper surface



(b) Lower surface



(c) Pressure and skin friction profiles

Figure 3 – Lift-to-drag maximization of the SBW100-NLF aircraft with 28° and 26° sweep.

Table 3 – Lift-to-drag maximization results of the SBW100-NLF aircraft with 24° sweep.

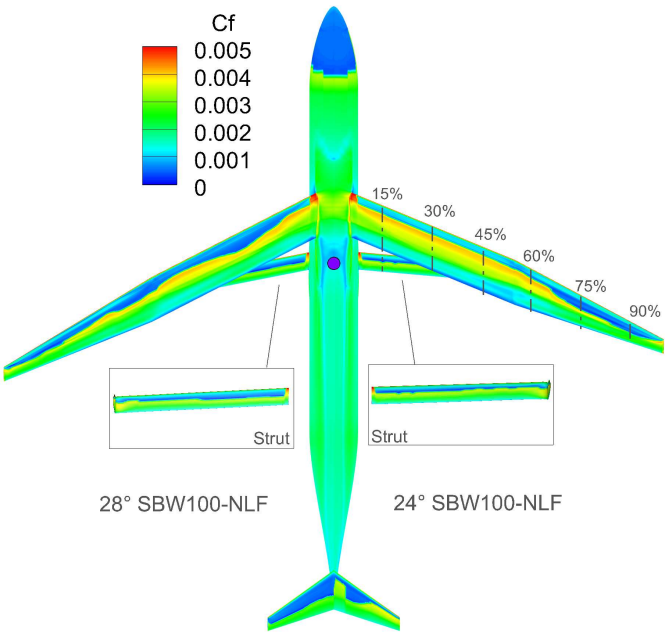
	D^1 [lb]	D_p [lb]	D_f [lb]	C_L	L [lb]	Altitude (ft)	L/D^1	AOA	Λ
SBW100 fully turbulent optimum	3,975	2,118	1,857	0.68	97,000	44,670	24.4	2.96°	30°
SBW100-NLF 28° Sweep	3,348	1,787	1,560	0.67	96,820	44,350	28.9	2.86°	28°
SBW100-NLF L/D maximization	3,358	1,885	1,473	0.72	96,510	45,800	28.7	2.11°	24°
SBW100-NLF / SBW100 turbulent	-15.5%	-11.0%	-20.7%	-	-490	+1,130	+17.6%	-	-
SBW100-NLF / SBW100-NLF 28° Sweep	+0.3%	+5.5%	-5.6%	-	-310	+1,450	-0.70%	-	-

[1] Excrescence drag markup and drag contributions from the vertical tail, nacelles, and pylons are not included.

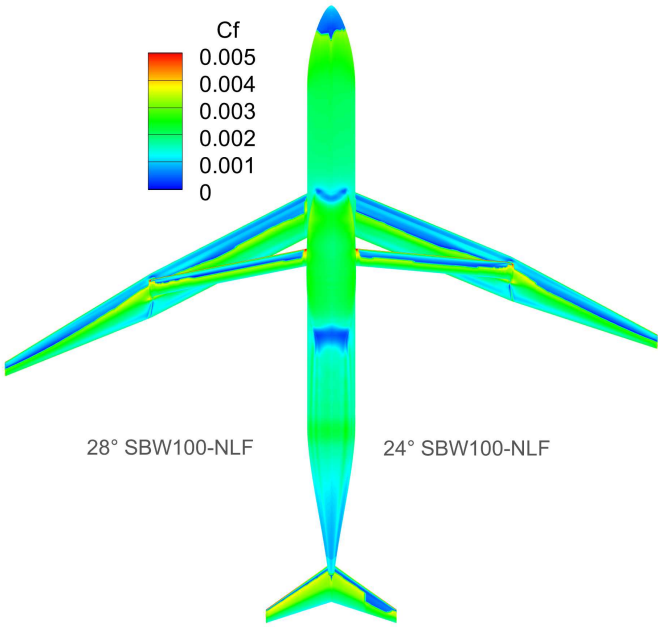
Table 4 – Lift-to-drag maximization results of the SBW100-NLF aircraft with 22° sweep.

	D^1 [lb]	D_p [lb]	D_f [lb]	C_L	L [lb]	Altitude (ft)	L/D^1	AOA	Λ
SBW100 fully turbulent optimum	3,975	2,118	1,857	0.68	97,000	44,670	24.4	2.96°	30°
SBW100-NLF 28° Sweep	3,348	1,787	1,560	0.67	96,820	44,350	28.9	2.86°	28°
SBW100-NLF L/D maximization	3,344	1,875	1,469	0.71	96,380	45,700	28.8	2.03°	22°
SBW100-NLF / SBW100 turbulent	-15.9%	-11.5%	-20.9%	-	-620	+1,030	+18.0%	-	-
SBW100-NLF / SBW100-NLF 28° Sweep	-0.1%	+4.9%	-5.9%	-	-440	+1,350	-0.35%	-	-

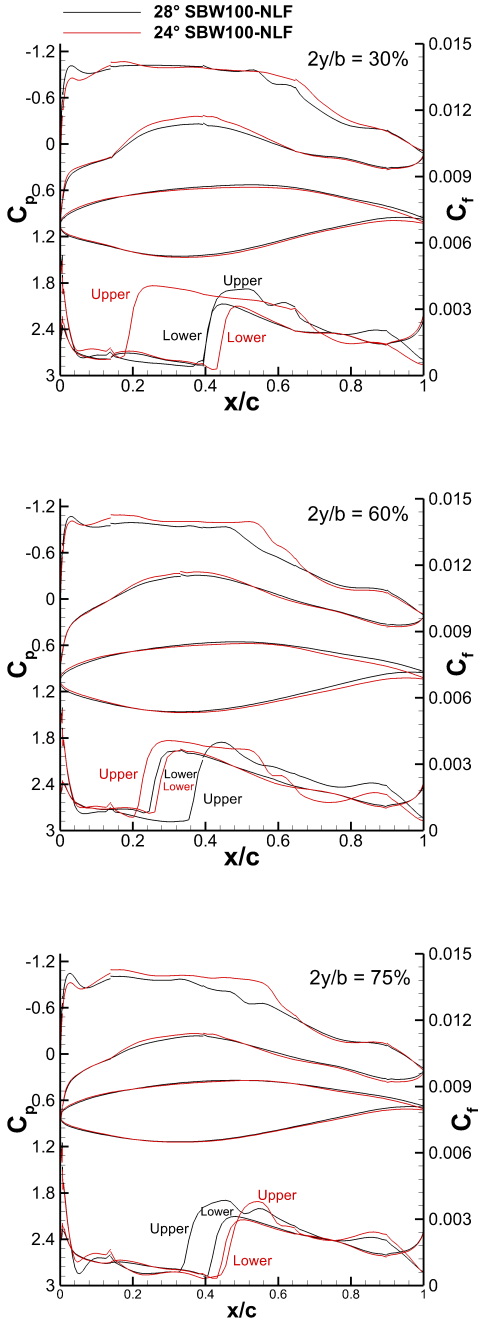
[1] Excrescence drag markup and drag contributions from the vertical tail, nacelles, and pylons are not included.



(a) Upper surface

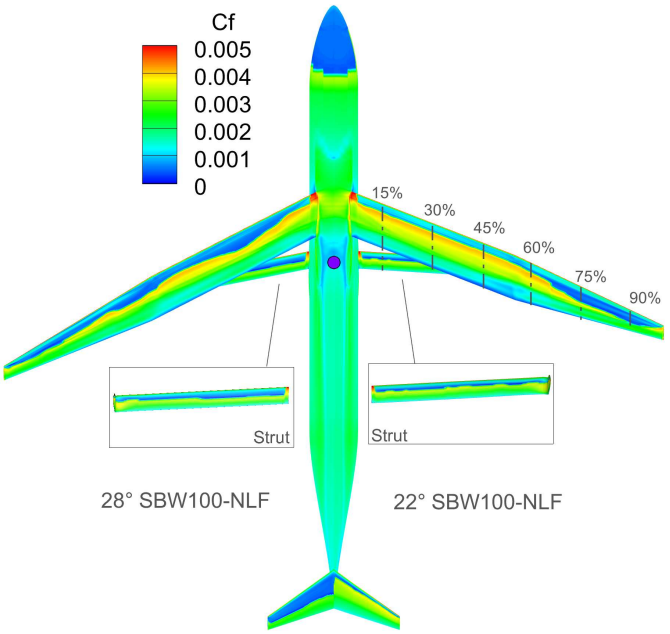


(b) Lower surface

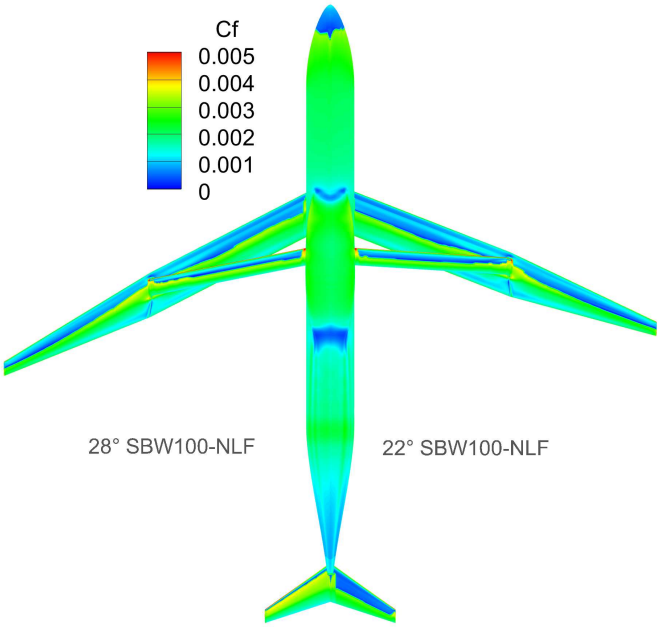


(c) Pressure and skin friction profiles

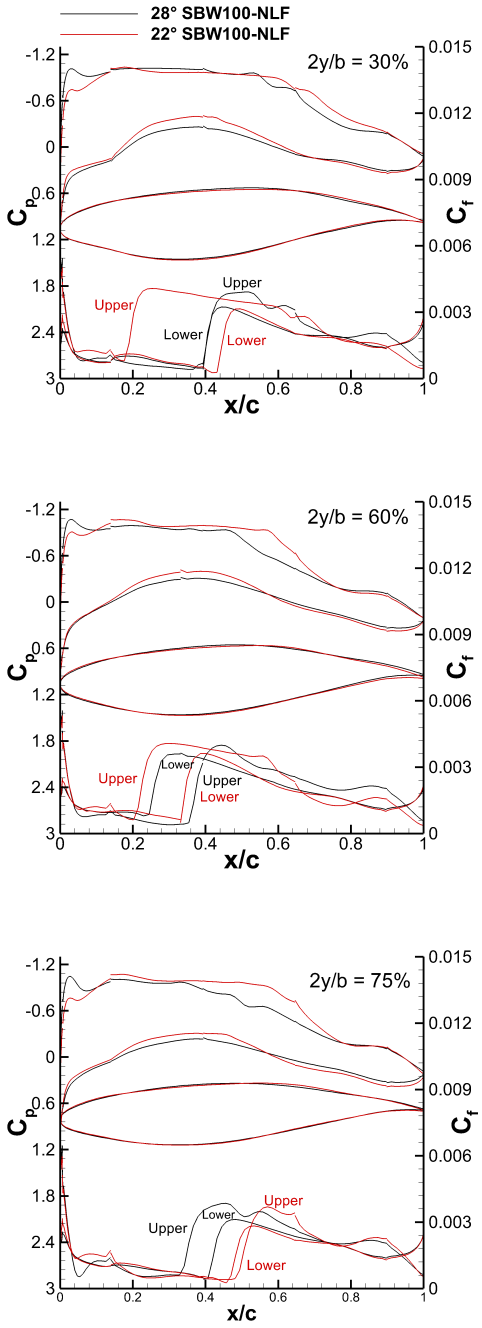
Figure 4 – Lift-to-drag maximization of the SBW100-NLF aircraft with 28° and 24° sweep.



(a) Upper surface



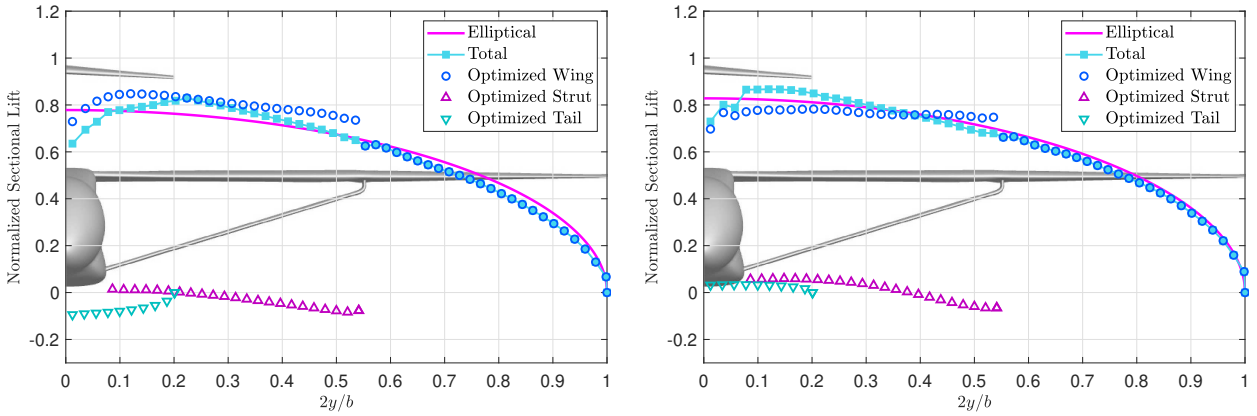
(b) Lower surface



(c) Pressure and skin friction profiles

Figure 5 – Lift-to-drag maximization of the SBW100-NLF aircraft with 28° and 22° sweep.

cases in Figure 6. Outboard of the wing-strut junction, the net lift distribution for both cases closely follows an elliptical distribution, with closer agreement observed for the 22° case. Similarly, inboard of the wing-strut junction, the 22° case shows better agreement with the elliptical distribution. In the 28° case, the inboard wing generates higher lift than in the 22° case to compensate for the larger negative lift generated by the horizontal tail. As the sweep angle is reduced, the tail incidence angle becomes less negative and eventually positive in the 22° case. This results in a reduction in tail downforce at trim, culminating in positive lift in the 22° case, primarily driven by the forward movement of the wing center of pressure associated with reduced wing sweep. In addition, part of the strut contributes to positive lift as the sweep angle is reduced.



(a) 28° sweep (b) 22° sweep

Figure 6 – Spanwise lift distributions of the SBW100-NLF aircraft.

Table 5 – Lift-to-drag maximization results of the SBW100-NLF aircraft operating at cruise speed of Mach 0.78.

	D [lb]	D_p [lb]	D_f [lb]	C_L	L [lb]	Altitude (ft)	L/D	AOA
30° SBW100 fully turbulent optimum	3,975	2,118	1,857	0.68	97,000	44,670	24.4	2.96°
L/D maximizations:								
28° SBW100-NLF	3,348	1,787	1,560	0.67	96,820	44,350	28.9	2.86°
26° SBW100-NLF	3,355	1,856	1,499	0.70	96,660	45,300	28.8	2.24°
24° SBW100-NLF	3,358	1,885	1,473	0.72	96,510	45,800	28.7	2.11°
22° SBW100-NLF	3,344	1,875	1,469	0.71	96,380	45,700	28.8	2.03°
28° SBW100-NLF / 30° SBW100	**-15.8%**	-15.6%	-16.0%	-	-180	-320	+18.5%	-
26° SBW100-NLF / 30° SBW100	**-15.6%**	-12.4%	-19.3%	-	-340	+630	+18.0%	-
24° SBW100-NLF / 30° SBW100	**-15.5%**	-11.0%	-20.7%	-	-490	+1,130	+17.6%	-
22° SBW100-NLF / 30° SBW100	**-15.9%**	-11.5%	-20.9%	-	-620	+1,030	+18.0%	-

4. Summary and Conclusions

A study of the impact of wing sweep angle on the performance of a strut-braced-wing configuration with natural laminar flow has been presented. A summary of the results is shown in Table 5, highlighting the performance benefits of the SBW100-NLF aircraft at various sweep angles relative to the baseline SBW100 configuration under fully turbulent flow conditions. Optimal SBW100-NLF configurations with sweep angles varying between 28° to 22° yield similar cruise drag when operating at a transonic cruise speed of Mach 0.78, more than 15% lower than an equivalent strut-braced-wing aircraft optimized and analyzed under fully turbulent conditions. The optimal altitude of the 28° sweep angle configuration is found to be 44,350 ft, while further reducing the sweep angle beyond 28° drives the optimal altitude higher and increases the extent of laminar flow, primarily over the lower wing surface. In combination with the reduced dynamic pressure from the lower density at higher altitudes, the skin-friction drag is reduced with decreasing sweep angle; however, pressure drag increases due to a combination of stronger shocks at pressure recovery and reduced density.

Investigations of off-design cruise conditions for the SBW100-NLF aircraft, with variations in cruise speed and aircraft weight will be explored in future work. For the fully turbulent SBW100 aircraft, Chau and Zingg [22] analyzed their single-point optimum at five off-design cruise conditions, and noted performance degradation relative to the nominal cruise design point of Mach 0.78 and lift coefficient of 0.68. This was due to the introduction of shocks, primarily when increasing the cruise speed and lift coefficient. They improved the robustness of their SBW100 aircraft through a multipoint optimization that accounted for all five cruise conditions, without compromising performance at the nominal design point. Preliminary investigations of the SBW100-NLF with 28° sweep at off-design conditions also indicate the introduction of shocks that degrade the performance of the aircraft relative to the on-

design cruise conditions of Mach 0.78 and lift coefficient of 0.67. However, the transition location does not appear to be negatively affected when operating at varying cruise conditions. Nevertheless, similar to the fully turbulent SBW100, performance degradation motivates a multipoint optimization to improve the robustness of the SBW100-NLF aircraft.

5. Contact Author Email Address

mailto: nathalie.saadeh@mail.utoronto.ca

6. Copyright Statement

The authors confirm that they, and/or their company or organization, hold copyright on all of the original material included in this paper. The authors also confirm that they have obtained permission, from the copyright holder of any third party material included in this paper, to publish it as part of their paper. The authors confirm that they give permission, or have obtained permission from the copyright holder of this paper, for the publication and distribution of this paper as part of the ICAS proceedings or as individual off-prints from the proceedings.

References

[1] Pfenninger Werner. Long-range LFC transport. *NASA, Langley Research Center, Research in Natural Laminar Flow and Laminar-Flow Control, Part 1*, 1987.

[2] Gern Frank, Ko Andy, Grossman Bernard, Haftka Rafael, Kapania Rakesh, Mason William, and Schetz Joseph. Transport Weight Reduction Through MDO: The Strut-Braced Wing Transonic Transport. In *35th AIAA Fluid Dynamics Conference and Exhibit*. AIAA Paper 2005-4667.

[3] Chau Timothy and Zingg David W. Aerodynamic Design Optimization of a Transonic Strut-Braced-Wing Regional Aircraft. *Journal of Aircraft*, 59(1):253–271, 2022.

[4] Malik Mujeeb, Liao Wei, Li Fei, and Choudhari Meelan. Discrete-Roughness-Element-Enhanced Swept-Wing Natural Laminar Flow at High Reynolds Numbers. *AIAA Journal*, 53(8):2321–2334, 2015.

[5] Bradley Marty K, Droney Christopher K, and Allen Timothy J. Subsonic Ultra Green Aircraft Research. Phase II-Volume I; Truss Braced Wing Design Exploration. *National Aeronautics and Space Administration, Langley Research Center*, April 2015. NASA/CR-2015 218704/Volume I.

[6] Sa'adeh Nathalie, Chau Timothy, and Zingg David W. Aerodynamic Shape Optimization of a Transonic Strut-Braced-Wing Regional Jet With Natural Laminar Flow. In *AIAA SCITECH 2026 Forum*. AIAA Paper 2026-0868, 2026.

[7] Hicken Jason E and Zingg David W. Aerodynamic Optimization Algorithm with Integrated Geometry Parameterization and Mesh Movement. *AIAA Journal*, 48(2):400–413, 2010.

[8] Gagnon Hugo and Zingg David W. Two-Level Free-Form and Axial Deformation for Exploratory Aerodynamic Shape Optimization. *AIAA Journal*, 53(7):2015–2026, 2015.

[9] Osusky Michal and Zingg David W. Parallel Newton–Krylov–Schur Flow Solver for the Navier–Stokes Equations. *AIAA Journal*, 51(12):2833–2851, 2013.

[10] Piotrowski Michael GH and Zingg David W. Smooth Local Correlation-Based Transition Model for the Spalart–Allmaras Turbulence Model. *AIAA Journal*, 59(2):474–492, 2021.

[11] Spalart Philippe and Allmaras Steven. A One-Equation Turbulence Model for Aerodynamic Flows. In *30th AIAA Aerospace Sciences Meeting and Exhibit*. AIAA Paper 1992-439.

[12] Gill Philip E, Murray Walter, and Saunders Michael A. SNOPT: An SQP Algorithm for Large-Scale Constrained Optimization. *SIAM Review*, 47(1):99–131, 2005.

[13] Osusky Lana, Buckley Howard, Reist Thomas, and Zingg David W. Drag Minimization Based on the Navier–Stokes Equations using a Newton–Krylov Approach. *AIAA Journal*, 53(6):1555–1577, 2015.

[14] Hicken Jason E and Zingg David W. Parallel Newton–Krylov Solver for the Euler Equations Discretized Using Simultaneous Approximation Terms. *AIAA Journal*, 46(11):2773–2786, 2008.

[15] Piotrowski MGH and Zingg DW. Compressibility Corrections to Extend a Smooth Local Correlation-Based Transition Model to Transonic Flows. *The Aeronautical Journal*, 127(1313):1141–1170, 2023.

[16] Langtry Robin. Extending the $\gamma - \tilde{Re}_{\theta t}$ Correlation Based Transition Model for Crossflow Effects. In *45th AIAA Fluid Dynamics Conference*. AIAA Paper 2015-2474, 2015.

[17] Langtry Robin B and Menter Florian R. Correlation-Based Transition Modeling for Unstructured Parallelized Computational Fluid Dynamics Codes. *AIAA Journal*, 47(12):2894–2906, 2009.

[18] Nocedal Jorge and Wright Stephen J. *Numerical Optimization*. Springer, 1999.

[19] Jameson Antony, Martinelli Luigi, and Pierce Niles A. Optimum Aerodynamic Design using the Navier–Stokes Equations. *Theoretical and Computational Fluid Dynamics*, 10(1):213–237, 1998.

[20] Embraer S.A. *E-Jets E2 Airport Planning Manual*, 2017. Revision 12 - 08. February 2019.

[21] Raymer Daniel P. *Aircraft Design: A Conceptual Approach*. AIAA Education Series. American Institute of Aeronautics and Astronautics, 5 edition, 2012.

[22] Chau Timothy and Zingg David W. Fuel Burn Evaluation of a Transonic Strut-Braced-Wing Regional Aircraft Through Multipoint Aerodynamic Optimisation. *The Aeronautical Journal*, 127(1308):305–329, 2023.